INSTITUTE OF PHYSICS PUBLISHING and INTERNATIONAL ATOMIC ENERGY AGENCY NUCLEAR FUSION

Nucl. Fusion **43** (2003) 107–118 PII: S0029-5515(03)57534-2

Magnetic topology of a candidate NCSX plasma boundary configuration

A.E. Koniges, A. Grossman[1], M. Fenstermacher, J. Kisslinger[2], P. Mioduszewski[3], T. Rognlien, E. Strumberger[2] and M. Umansky

Lawrence Livermore National Laboratory, Livermore, CA 94550, USA
[1] University of California, San Diego, La Jolla, CA, USA
[2] Max-Planck-Institut fur Plasmaphysik, Garching, Germany
[3] Oak Ridge National Laboratory, Oak Ridge, TN 37831, USA

Received 19 April 2002, accepted for publication 2 December 2002
Published 15 January 2003
Online at stacks.iop.org/NF/43/107

Abstract
A candidate magnetic topology of the plasma boundary of the proposed compact stellarator national compact stellarator experiment (NCSX) is investigated using field-line tracing with diffusion. The required magnetic fields are obtained from a free-boundary equilibrium using the magnetic fields from external coils and bootstrap plasma currents inside the last closed magnetic surface (LCMS). These results are used to calculate the magnetic fields of the finite beta equilibria inside and outside the LCMS in a form suitable for field-line tracing. Poincaré plots of field lines that diffuse outwards from starting points just inside the LCMS indicate an ergodic divertor region. Intersections of field lines with a simple limiting surface show contained patches suitable for divertor control. Undesirable regions of sharply inclined angle of intersection with the limiting surface are localized, indicating the suitability of the configuration for optimized divertor design techniques. We also discuss physics implications of field-line lengths in the divertor region.

PACS numbers: 52.55.Hc

1. Introduction

Power and particle handling in the proposed national compact stellarator experiment (NCSX) is achieved by providing controlled target surfaces for plasma–wall interactions. The location of these surfaces is determined by the interplay of practical issues such as the placement of diagnostic ports and coil locations and by the requirements of the confined plasma equilibrium configuration. In this paper, we present a detailed analysis of one such equilibrium configuration to determine the diversion properties of the magnetic field and thus develop a divertor concept for the NCSX. In doing so, we describe a procedure for expediting three-dimensional field-line tracing enhanced with simulated cross-field diffusion. Similar calculations for other three-dimensional devices such as W7-X [1–5], have been central to determining the final device configuration and the placement of limiters or divertor plates, and other plasma-facing components.

To determine the magnetic topology of the plasma boundary region, we adopt the methodology developed for W7-X [6]. Namely, we start with an equilibrium solution calculated from the external coils and the bootstrap current as computed by the energy minimizing variational moments equilibrium code (VMEC) [7], which assumes the existence of nested flux surfaces. It determines the Fourier coefficients of the nested flux surfaces and of the magnetic field in the three-dimensional geometry up to the last closed magnetic surface (LCMS). Coupling of the VMEC solution to the magnetic field solver for finite-beta equilibrium (MFBE) code [6], allows one to determine the magnetic field on a three-dimensional grid for the entire region of interest, including the scrape-off layer (SOL) outside the LCMS. For W7-X, field-line tracing with diffusion was considered to be the basic method for investigating the flow of energy and particles outside the confinement region [1–5, 8]. It is then possible to study the properties of the magnetic field in detail and determine the diversion requirements. For W7-X, this basic 'diversion structure' consisted of plasma boundary magnetic field lines intersecting a control surface surrounding the plasma with a pattern of helical strips following the helical edges [1, 8].

In this paper we study a specific example representative of the NCSX standard configuration. We determine the intersection of the field lines with a limiting surface that toroidally surrounds the plasma. The surface is not itself conformal to the LCMS, nor is it intended to represent the vacuum vessel. Instead, the limiting surface is the proposed plasma-facing components surface of all protective armour including the divertor, which might be mounted inside the vacuum vessel. Detailed studies of a range of possible coil configurations for NCSX and their magnetic configurations outside the LCMS are presented elsewhere [9].

 © 2003 IAEA, Vienna Printed in the UK

This paper is organized as follows. In section 2, we review the geometrical properties of the NCSX device, the limiting surface, and the reference calculations from VMEC and MFBE that provide the starting point for our investigations. In section 3 we describe a methodology developed for W7-X that allows a large number of field lines to be traced in a rapid fashion giving a complete picture of the diversion region of the plasma. In these calculations, diffusion of the field lines is introduced at varying levels to mimic the diffusive behaviour of plasma particles or energy transport due to small-scale turbulence. In section 4, we provide results of our calculations including three-dimensional 'footprints' or signatures of the field-line intersection pattern on the limiting surface. We also give details of the diffused field-line length for the intersecting lines and inclination angle of intersection with the surface. In section 5 we give some theoretical insight and one-dimensional calculations of field-line length effects in the diversion region. Finally, in section 6 we conclude and give recommendations for divertor design.

2. Geometrical aspects and reference calculations

NCSX is planned as a low aspect ratio, high-beta quasi-axisymmetric stellarator with three field periods [10]. The goal of the NCSX team is to design a compact device with good transport and stability properties. The reference design for initial physics optimization, called li383, is based on a high-beta regime ($\beta = 4\%$). The equilibrium properties of li383, such as the rotational transform are presented elsewhere [11]. Unlike other stellarator devices where the vacuum fields are quite useful for the study of the divertor and SOL regions, the NCSX configuration relies on the bootstrap current and, thus, finite beta as an essential element of the design. Thus, we use this $\beta = 4\%$ reference design as a basis for our investigations. Our detailed studies should provide a baseline for further optimization of the divertor and baffle plate geometry.

For the purpose of determining the location of protective armour, a limiting surface has been defined for NCSX and introduced into the NCSX database [10]. Initially, this surface was chosen to be just a constant distance of 2 cm away from the bounding plasma as determined by a VMEC fixed boundary analysis. As the engineering design evolved, however, it became apparent that to allow for the use of neutral beams it was necessary to pull out the surface even further at the outboard midplane of the kidney section ($\phi = 0$). This optimized surface (vvfw_surf.li383_1.4m) is used in our design study. For quantitative analysis, this surface is described by a Fourier coefficient representation based on the NESCOIL convention, i.e.

$$r = \sum_{m,n} R_{mn} \cos(m\theta + n\phi),$$

$$z = \sum_{m,n} Z_{mn} \sin(m\theta + n\phi),$$

that can be inverted to give the (r, z)-coordinates. Here, ϕ is the toroidal angle, θ is the poloidal angle, and R_{mn} and Z_{mn} are the Fourier coefficients. A table of the Fourier coefficients is included as an appendix. We note that the final position of such a bounding surface will depend on engineering issues associated with divertor plates as well as optimization of the plasma configuration via studies such as this present work.

To facilitate field-line tracing calculations (as well as other equilibrium studies) in finite-beta equilibria, including contributions from the coils and the equilibrium plasma state, the MFBE code was developed [6]. This code, used together with the VMEC2000 code for self-consistent calculations, calculates a continuous representation of the magnetic field at equally spaced grid points in a three-dimensional space both inside and outside the LCMS. Recently, MFBE was modified to include computations of equilibria with non-vanishing toroidal current, e.g. bootstrap current. The numerical method used there is based on the so-called 'virtual casing' principle [12] which also allows the computation of magnetic fields of equilibria with net toroidal current, such as quasi-axisymmetric and tokamak equilibria [13].

Before discussing our field-line tracing calculations where diffusion is included and the wall footprints are calculated, we give details of the reference MFBE solution. Figures 1 and 2 show the Poincaré section data for the li383 NCSX case for a series of cross sections from 0° to 70° in toroidal angle. In these plots, field lines are started at a series of equally spaced points marching radially outwards on the midplane of the cross section at toroidal angle $\phi = 60°$. Each of these starting points is followed for a total of 120 transits in the toroidal direction and Poincaré plots are retained at 10° intervals. The nested closed flux surface plasma region inside the LCMS is illustrated with the green-coloured points starting at the plasma centre and moving outwards, towards the VMEC plasma boundary denoted by a red curve on each plot. The limiting surface for each of these cross sections is given by a blue dashed curve. This limiting surface is not used in these reference calculations; it is only shown so that we can refer to its location in the following sections. Finally, a few Poincaré section points for varying poloidal radii, also in green, indicate the ergodic region outside the plasma.

One notable aspect of the plots in figures 1 and 2 is the rapid degradation of the nested nature of the flux surfaces leading to a highly ergodic SOL region. Thus, a careful study of the region outside the LCMS is required to determine the actual footprints or intersections of the field-line transit paths with the limiting wall. This leads us to the technique for mapping the region between the LCMS and the wall as described in the next section.

3. Methodology: field-line tracing with diffusion

A first step in designing a divertor/limiter is to map out the 'footprint' of the plasma (i.e. the intersection pattern of the field lines in toroidal/poloidal space) in the SOL region either on a conformal surface or a limiting wall. Since we have in hand a specification of a limiting wall, we can trace field lines and determine where these lines intersect the limiting surface. Then, more detailed divertor locations can be specified and optimized to constrain the size of the footprint, thereby, reducing or eliminating the fraction of field lines that intersect the limiting surface in undesirable locations or with greater inclination angle. It is important to realize that diverting the plasma in one location can affect the plasma footprint in other locations.

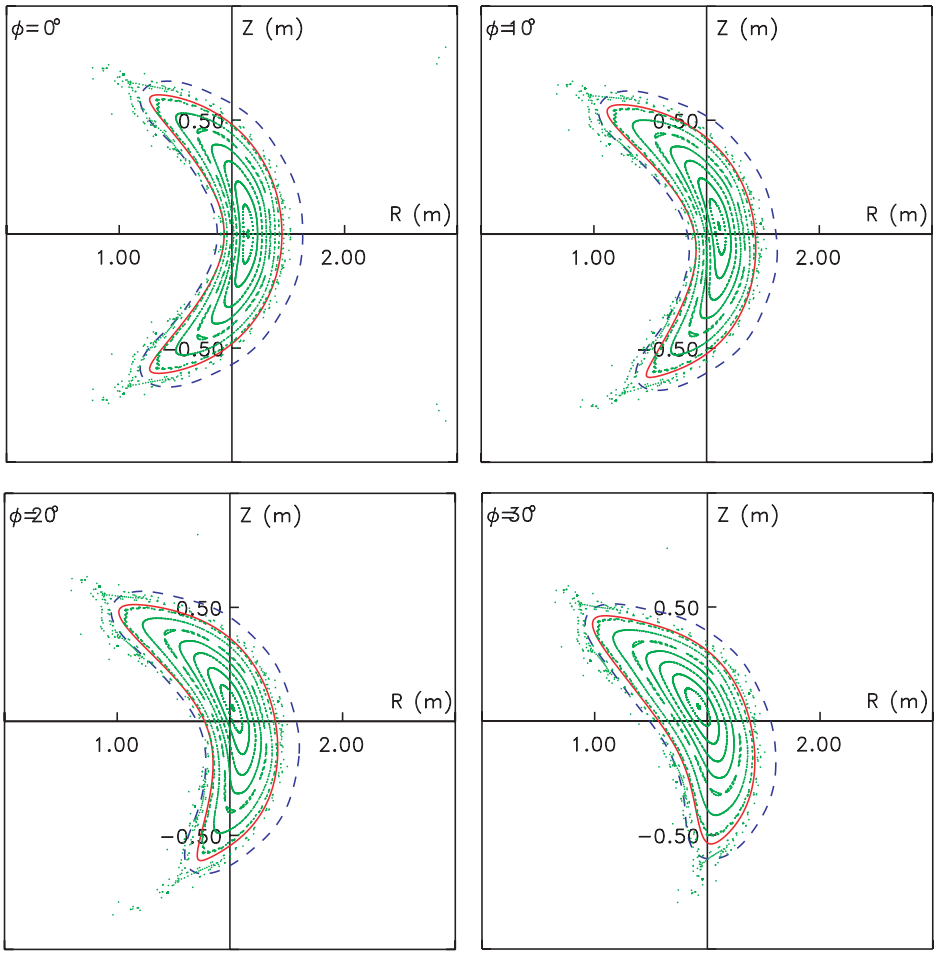

Figure 1. Poincaré plots (in green) for MFBE solutions at 0–30°. The VMEC plasma boundary is shown as a red curve, and the limiting wall is shown as a blue dashed curve.

Field-line tracing paths that are started outside the NCSX LCMS appear to be ergodic and diverge very quickly from a regular nested pattern. Furthermore, field lines that are traced by starting a significant distance outside the region of closed surfaces may not be realistic if their starting points are such that they could not be attained by a plasma appropriately contained by a limiting surface and undergoing normal cross-field diffusion. Thus, we use the following algorithm as a basis for our choosing appropriate field-line tracing starting points for calculating footprints. This method allows us to adequately cover the ergodic region between the LCMS and the wall without introducing spurious solutions that could not be reached by natural cross-field diffusion. We first define a 'starting surface' by integrating a field-line path just inside the LCMS. To ensure complete coverage, a linear interpolation of these points is used to obtain a new set of starting points that correspond to more than one single starting surface. Triangular points in figure 3 depict a sample set of new starting points. In this view, one can see that the triangular starting points cover the poloidal extent. Field-line tracing with diffusion is started from this initial set. To move the points away from the more nested solutions inside the LCMS, a cross-field diffusion is introduced as follows.

Cross-field diffusion in a stellarator is assumed to be anomalous and of the order of $10^4\,\mathrm{cm}^2\,\mathrm{s}^{-1}$ [14]. To simulate the SOL diffusion numerically, we introduce 'diffusion' of field lines in our integration techniques. Here, the diffusion coefficient, D, is given by

$$D = \Delta^2 \frac{V_\mathrm{T}}{\lambda},$$

where Δ is the maximum displacement introduced during field-line tracing, λ is a characteristic length, and V_T is a thermal velocity (here, $V_\mathrm{T} = 3.17 \times 10^7\,\mathrm{cm\,s}^{-1}$). In each toroidal integration step, a random change up to a maximum of Δ in the R- and Z-coordinates of the point is calculated. Here, the characteristic length is equal to the average arc length between the toroidal angles where the field is specified. Thus, a larger time interval associated with a larger field-line spacing gives the position a larger random kick and the end result is that the amount of diffusion is independent of the field spacing. The direction of the diffusive kick is random, so the field line may diffuse either inwards or outwards. Numerical reflecting limiters, that serve to speed the calculation, eventually stop field lines that diffuse inwards. These limiters are placed several orders of magnitude further away than a characteristic diffusion length and their precise location does not affect the final results. Field lines that diffuse outwards are followed until a specified maximum calculation time is reached or until the field-line path intersects the limiting surface. Once field-line integration is stopped, either by intersecting the numerical

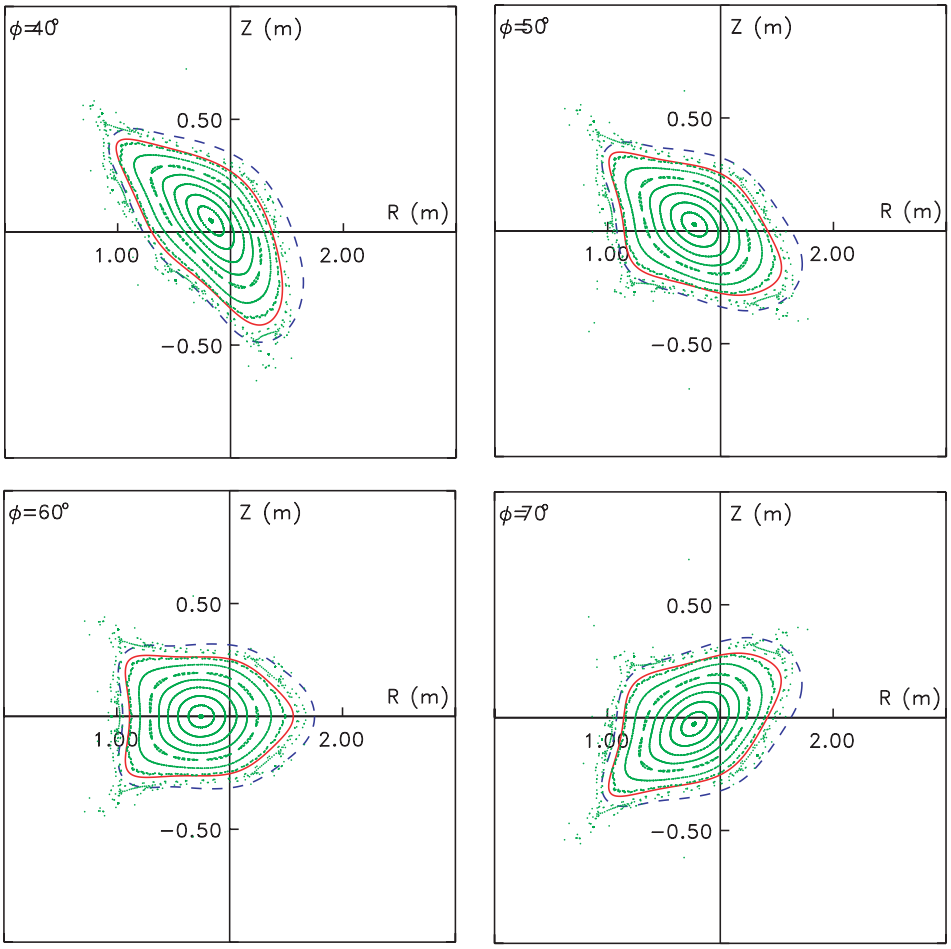

Figure 2. Poincaré plots (in green) for MFBE solutions at 40–70°. The VMEC plasma boundary is shown as a red curve, and the limiting wall is shown as a blue dashed curve.

inner reflectors or by intersecting the outer limiting surface, a new starting point is determined as a perturbation of the initial starting surface. A close-up sample of new starting points is depicted in figure 4.

4. Results

The magnetic field structure outside the LCMS is studied using the methodology described in the previous section, whereby a large number of field lines are followed including diffusive effects. The key point in obtaining good plasma performance in the NCSX is to implement edge control with divertor-like configurations. In order to design the divertor region, we must understand the boundary configuration. In particular, we study the SOL region of the plasma between the LCMS and the limiting surface via Poincaré plots, intersections of field lines with the limiting surface, and the confinement properties of the plasma, namely the connection length.

4.1. Poincaré plots

In figure 5, we show sample Poincaré plots for a toroidal angle $\phi = 0^\circ$ with diffusion included. View A shows the punctures with the limiting surface included, and view B shows the calculation with no limiting surface. In both views, 10 000 sample punctures of the plane are plotted. Radial field-line expansion at the tips of the banana shape shows promise for localized divertor operation.

In the analyses and results that follow, we have considered two cases, moderate diffusion where $D = 1.0 \times 10^4\,\mathrm{cm^2\,s^{-1}}$ and low diffusion where $D = 2.0 \times 10^3\,\mathrm{cm^2\,s^{-1}}$. However, for these Poincaré plots the differing values of D are indistinguishable from each other—the specific points are different but the general appearance of the picture is not.

Figure 6 shows Poincaré plots of the limited plasma at toroidal intervals spaced 10° apart starting from $\phi = 10^\circ$ through $\phi = 60^\circ$, thus, combined with figure 5, spanning one symmetry section of the three period geometry with stellarator symmetry.

4.2. Footprints

The Poincaré plots in figures 5 and 6 are just snapshots in time of the entire calculation where intersections with the limiting surface or 'footprints' are calculated. To obtain the intersection data, the calculation is continued until roughly 10 000–15 000 intersections with the limiting surface that define the 'footprint' are calculated. After an intersection, the field-line integration is restarted by the random perturbation to the initial starting surface point described in the previous section.

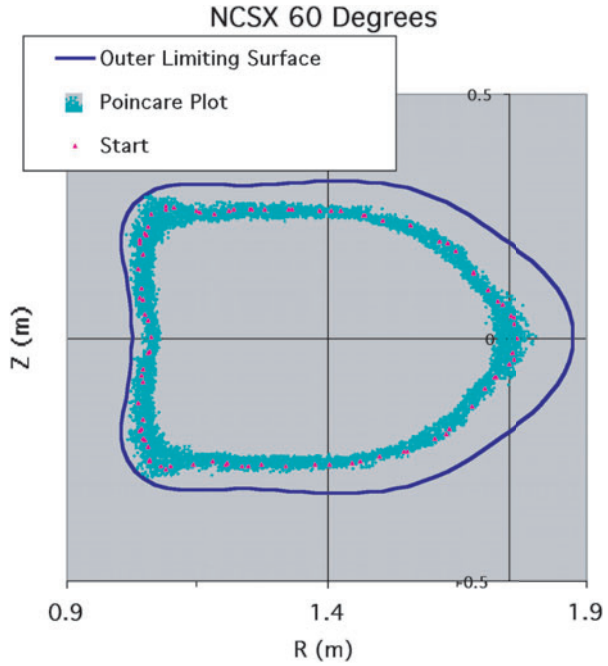

Figure 3. Starting surface points shown as red triangles superimposed on a Poincaré surface plot. (Details of the Poincaré surface plot points are given in the next section.) The position of the limiting surface is given by a blue curve.

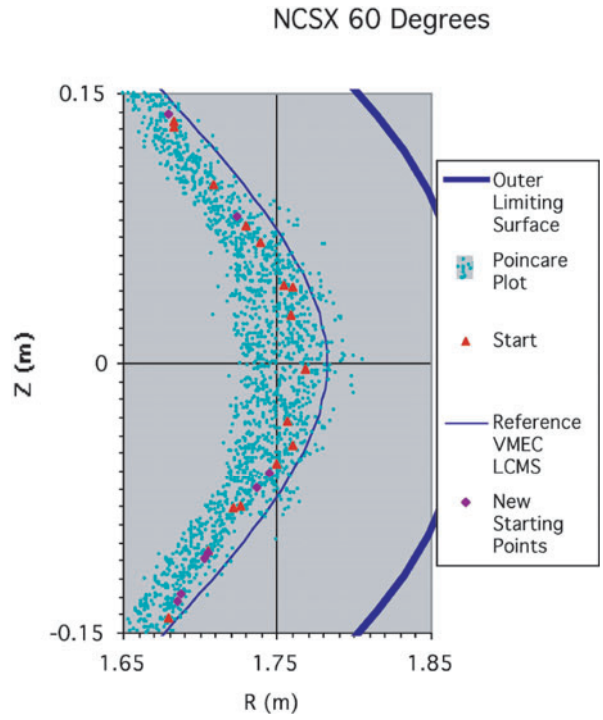

Figure 4. Close-up view of starting surface points (red triangles) superimposed on a Poincaré plot. Both VMEC plasma boundary and outer limiting surface positions are shown. New starting points are given as purple diamonds.

Three-dimensional plots of the intersection points are shown on a segment of the stellarator in figure 7. A moderate value of the diffusion coefficient $D = 1.0 \times 10^4\,\mathrm{cm}^2\,\mathrm{s}^{-1}$ is used for these results. (Two views of the same surface

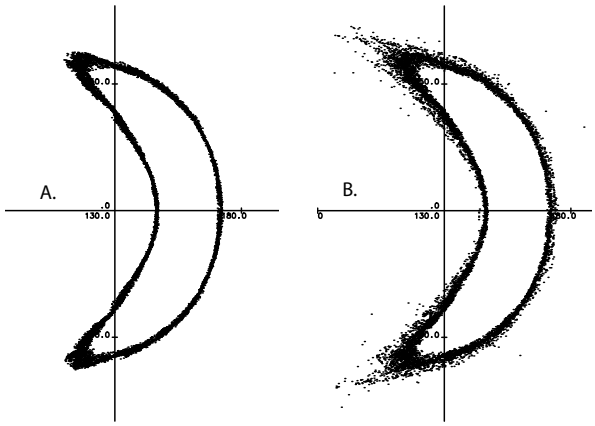

Figure 5. Poincaré plots $\phi = 0^\circ$ with a limiting surface (view A) and no limiting outside the LCMS (view B).

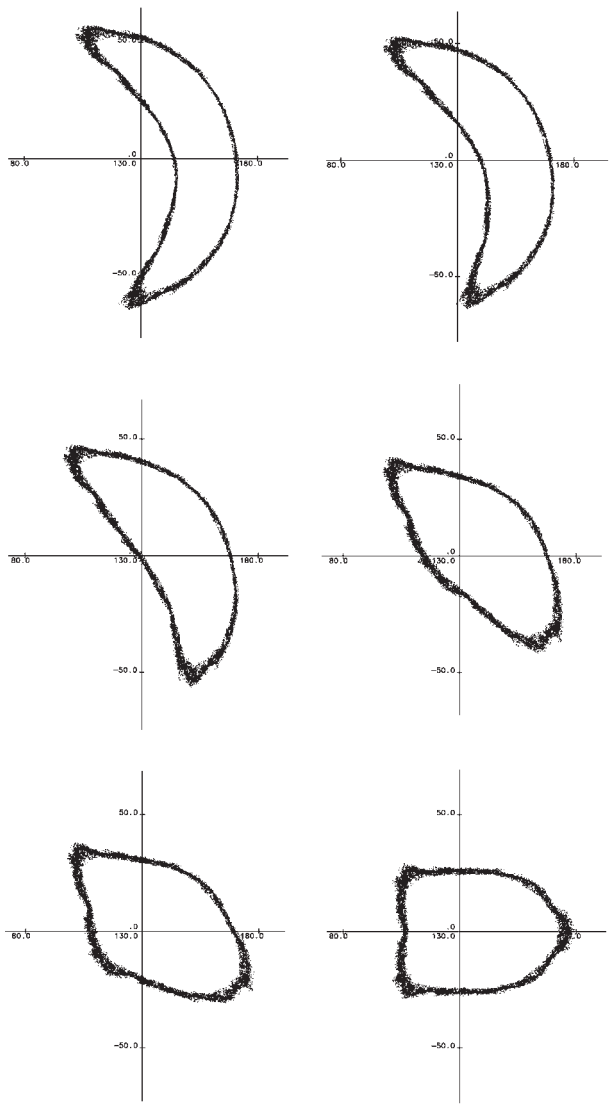

Figure 6. Sample Poincaré plots for field-line tracing with diffusion given at 10° intervals from 10° to 60°. The plasma (field line) is stopped by a limiting surface.

are rotated slightly to show the strike-point locations.) The limiting surface is represented in grey. Here, the stellarator is shown in a segment from $\phi = 0^\circ$ to 60° with the banana shaped cross section on the right-hand side. Since the stellarator has three periods and stellarator symmetry is assumed, this cut gives all the relevant information. In the plots, $\phi = 0^\circ$ is on the right-hand side and $\phi = 60^\circ$ is on the left-hand side. There are no intersection points on the back or outboard side of the device. The intersection points are colour-coded as to their inclination angle of intersection with the limiting surface. In this convention, intersecting the wall at normal incidence is 90° inclination. Here, the degrees of the intersection inclination are 12–15° red, 9°-12° green, 6–9° blue, 3–6° yellow, and 0–3° orange. In the design of the W7-X stellarator, no intersections with inclinational angle greater than 6° are permitted. This is done by further limiting of the plasma in the banana tips and other locations, thereby moving the strike points. As shown in the figure, the red points with the highest inclination angle occur at the 'D-shaped' cross section near 60°. Thus, as in W7-X it may be possible to move these strike points by additional limiting near the 0° cross section. (N.B. In the actual optimization process, one must refer to the data to be sure to optimize away the highest inclination angle points. Occasionally, since so many points are plotted, different intersection points may lie on top of each other masking the original colour code.)

Intersection or footprint data can also be represented on a toroidal/poloidal plot as in figure 8. Here, we show the intersection footprint pattern for the case of moderate diffusion with $D = 1.0 \times 10^4\,\mathrm{cm}^2\,\mathrm{s}^{-1}$. The plots show that there is a distinct footprint pattern repeated thrice, periodically. There are a few outlying points. For lower diffusion where $D = 2.0 \times 10^3\,\mathrm{cm}^2\,\mathrm{s}^{-1}$, the strike pattern is similar but there are less than 1000 intersections for the same amount of computer time. This indicates that the diffused field-line length, which is introduced in the following section, calculated

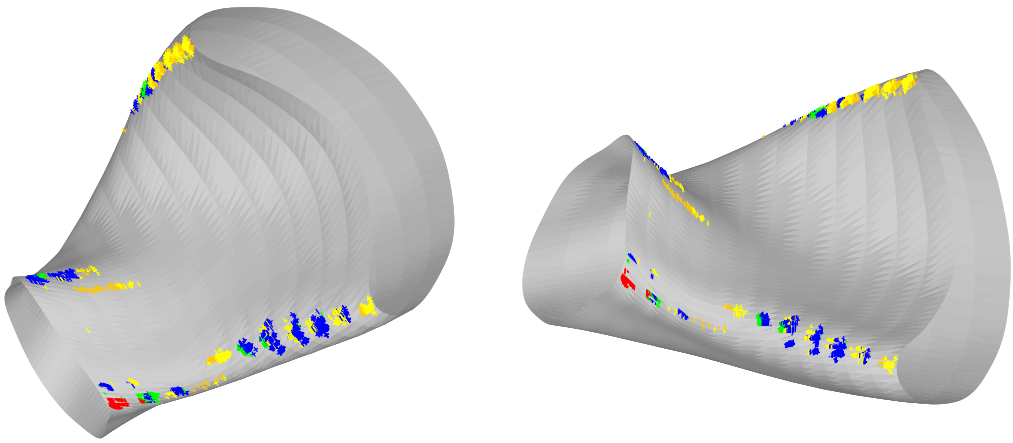

Figure 7. Segment of the limiting surface of the NCSX stellarator showing intersection points colour coded by inclination angle. The intersection points are colour coded with their inclination angle as 12–15° red, 9–12° green, 6–9° blue, 3–6° yellow, and 0–3° orange.

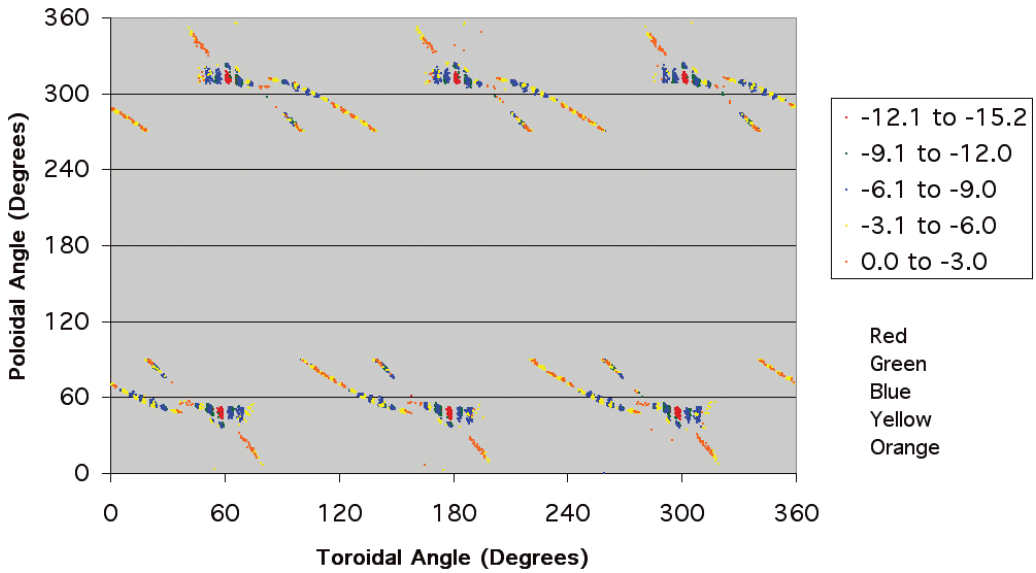

Figure 8. Strike-point locations in poloidal/toroidal space colour-coded with inclination angle of intersection.

by this procedure will depend significantly on D, i.e. it will be shorter for larger D. This is also quantified in the next section. When the simulation is run further to achieve approximately 10 000 intersections, the locations and the angles of inclination are not significantly different from the higher diffusion case. The only difference is that the number of outlying points (those that do not fit the repeating pattern closely) is reduced.

It is possible that highly energetic particles such as those produced by ELMs would have a much higher effective diffusivity than that studied here. Experiments performed after increasing the diffusivity to even higher levels show more outlying points, but the basic structure of the intersection patterns remain the same.

4.3. Diffused field-line length

The parallel connection length of the flux tube in which heat is conducted from the core plasma to the material surfaces is a quantity that strongly affects the temperature profile in the SOL and the resulting temperature near the targets. While we do not measure this quantity directly, we can have an indication of the results by considering the 'diffused field-line length,' namely the toroidal distance a traced particle travels from its starting point just inside the LCMS to the limiter strike point. In section 5 we discuss the implications of such a length and the implications for impurity generation and core plasma performance. In figure 9, we give a bar chart showing the length in metres of the orbit paths that strike the limiting wall. The values in the bar chart are binned according to the number of intersections out of a total of 13 069 calculated intersections. A moderate value of the diffusion coefficient $D = 1.0 \times 10^4\,\mathrm{cm^2\,s^{-1}}$ is used for these results.

Examination of the actual values plotted in figure 9 shows that more than 60% have a diffused field-line length of more than 100 m. This shows promise for the NCSX design. Furthermore, we note that the length values do not appear to be correlated with any of the other measured quantities such as toroidal/poloidal location or inclination angle of intersection. The average diffused line length for the moderate diffusion case is roughly a factor of two smaller than that of the lower diffusion case, namely 129 m and 229 m, respectively.

5. One-dimensional plasma modelling

The connection length, L_c, of field lines in the SOL outside the LCMS of NCSX is an important parameter that will determine the temperature profile of the SOL plasma. The L_c is related to the diffused field-line length discussed in the previous section, but L_c is generally defined as the $L/2$ of a field line traced backwards from the intersection with a limiter until its intersection with another limiter without diffusive effects perturbing the path. It will be possible to calculate this distance more accurately once the final NCSX configuration with limiters in place has been designated. Design choices under consideration now could have a dramatic effect on the magnitude of L_c. If L_c is too short the temperature profile along the field lines could be very flat with moderate to low temperature at both the target and separatrix. This might lead to thermal instabilities at the edge due to carbon cooling. Long connection length allows a high separatrix temperature, a significant temperature drop along field lines to a reasonably low target temperature, and establishment of a high recycling regime with low impurity source at the targets.

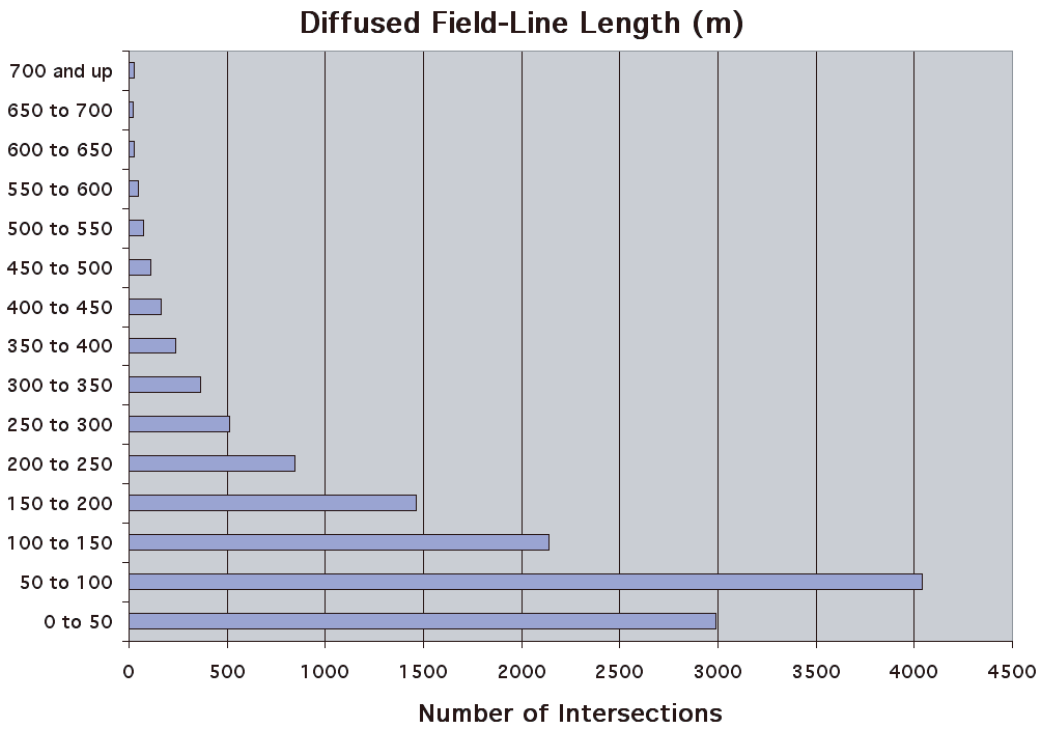

Figure 9. Diffused field-line length in metres binned according to number of intersections with that value out of a total of 13 069.

The upstream temperature may also be important because it is the boundary condition for the core temperature profile. Since NCSX is designed to have approximately the same drift orbits as a tokamak, the transport characteristics may be similar to tokamaks. In that case the separatrix temperature may set the height of the pedestal at the edge of the core plasma. If the temperature profiles are stiff inside the NCSX core plasma as in tokamaks, then the core energy content and confinement may be very sensitive to the separatrix temperature. If the transport is more like that in a classical stellarator then confinement improvement would still be expected at higher separatrix temperatures as seen in recent experiments [15, 16].

5.1. Basic equations of one-dimensional SOL parallel transport

Following Stangeby[4] [17] we look for solutions to the temperature profile in a SOL flux tube assuming parallel heat conduction dominates over convection. This has been shown to be a good assumption for the dominant electron channel in tokamaks except under detachment conditions in which the temperature is very low (∼1 eV) and the density is quite high (∼1×10^{20} m^{-3}). For non-detached SOL in NCSX, the Spitzer heat conductivity equation in the direction $s_{||}$ along the magnetic field from the LCMS to the wall is

$$\frac{\mathrm{d}[q_{||}]}{\mathrm{d}s_{||}} = \frac{\mathrm{d}[-K_0 T^{5/2}(\mathrm{d}T/\mathrm{d}s_{||})]}{\mathrm{d}s_{||}} = \frac{PG(s_{||})}{A_{||}}, \qquad (1)$$

where for a pure hydrogen plasma $K_{0e} \sim 2000$, $K_{0i} \sim 60$, T is in eV, and $s_{||}$ in m. The power from the core into the SOL is denoted as P, $G(s_{||})$ is a shape function whose $s_{||}$ integral gives unity, and $A_{||}$ is the area of the flux tube perpendicular to $\boldsymbol{B}$. Thus, $q_{||} = P/A_{||}$ for $A_{||}$ constant. For $T_e \sim T_i$, electron conduction dominates the parallel energy transport in the SOL, and at sufficient collisionality, the ion power is coupled through the electron channel via energy exchange collisions.

Assuming that the power enters the flux tube at only the upstream end (outer midplane where $s_{||} = 0$) or is uniformly distributed along the flux tube, only introduces a simple parameter α into the solution; $\alpha = 1$ for a localized source of $G(s_{||}) = \delta(s_{||})$ and $\alpha = 1/2$ for $G = 1/L_c$ [17]. Integrating the heat conduction equation thus gives the temperature at any point along the flux tube, $T_e(s_{||})$, in terms of either the upstream temperature, T_{eu}:

$$T_e(s_{||}) = \left[T_{eu}^{7/2} - \left(\frac{7\alpha}{2}\right)\left(\frac{P}{A_{||}}\right)\left(\frac{s_{||}}{K_{0e}}\right)\right]^{2/7}, \qquad (2)$$

or, in terms of the target temperature, T_{et}:

$$T_e(s_{||}) = \left[T_{et}^{7/2} + \left(\frac{7\alpha}{2}\right)\left(\frac{P}{A_{||}}\right)\left(\frac{L_c - s_{||}}{K_{0e}}\right)\right]^{2/7}. \qquad (3)$$

Upstream temperatures at least twice that of the target, can be well approximated by

$$T_{eu} = \left[\left(\frac{7\alpha}{2}\right)\left(\frac{P}{A_{||}}\right)\left(\frac{L_c}{K_{0e}}\right)\right]^{2/7}. \qquad (4)$$

[4] Compare pages 187 and 221.

In the evaluations given below, we set $\alpha = 1/2$ corresponding to uniform power deposition along the flux tube, but the solution does not depend very sensitively on it.

If one assumes that the sheath is the only heat sink in the SOL flux tube, i.e. there are no substantial radiation losses along the tube, and that parallel pressure balance holds owing to negligible cross-field transport of parallel momentum, then, stagnant flow upstream and Mach = 1 flow at the target allows one to express T_{et} in terms of power and upstream density, n_u, as

$$T_{et} = \left(\frac{m_i}{2e}\right)\left(\frac{2q_{||}}{\gamma e n_u}\right)^2\left(\frac{7\alpha q_{||} L_c}{2K_{0e}}\right)^{-4/7} \propto q_{||}^{10/7} n_u^{-2} L_c^{-4/7}. \qquad (5)$$

Here, $q_{||} = P/A_{||}$, and γ is the sum of energy sheath transmission factors for ions and electrons.

While equation (5) is useful for understanding the scaling trends when $T_{eu} > T_{et}$, the results presented in the examples below use the more general equation (3) rather than equation (4), so the specialized relations in (4) and (5) do not hold if $T_{eu} \approx T_{et}$. The generalized form of equation (5) for the target temperature is

$$T_{et} = \left(\frac{m_i}{2e}\right)\left(\frac{2q_{||}}{\gamma e n_u T_{eu}}\right)^2, \qquad (6)$$

which is solved numerically for T_{et} using equation (3) evaluated at $s_{||} = 0$.

5.2. NCSX examples

For estimating the NCSX target and upstream temperatures we use $K_{0e} = 2000$, $\gamma = 7$ and the following assumptions: (1) maximum input power to the core = 12 MW; (2) core radiation fraction = 0.2; (3) power entering the SOL = $12 \times 0.8 = 9.6$ MW; (4) SOL power scale width, $\lambda_{q\perp} = 2$ cm; (5) effective major and minor radii, $R_{eff} = 1.4$ m, $a_{eff} = 0.28$ m; (6) $A_{||}(\mathrm{SOL}) = 4\pi R \lambda_{q\perp}(B_\theta/B)$ (extra factor of 2 accounts for the two ends); (7) $(B_\theta/B) \sim 0.13$ for $\iota_{edge} \sim 0.65$. This leaves L_c, n_u, the ion species and the injected power as parameters. Note also that the target temperature in equation (5) scales as the SOL power scale width, $\lambda_{q\perp}$ to the $-10/7$ power, through $q_{||}^{10/7}$, so this is an important unknown parameter for NCSX. In the examples below we have used $\lambda_{q\perp} = 2$ cm as inferred from measurements on W7-AS [18].

5.2.1. Target and separatrix temperatures vs L_c and P_{inj}. To achieve low target sputtering and a high recycling regime in tokamaks one usually tries to minimize the plasma temperature near the targets while keeping the plasma from detaching. This means a T_{et} in the range of 10–20 eV. From figure 10 this low target temperature is reached in a deuterium plasma for the short L_c case only at very low input power, P_{inj} ∼1–2 MW. Figure 11 then shows that the upstream temperature will be about 30–40 eV. Higher input power raises the upstream temperature but the target temperature also increases. For the full 12 MW case in NCSX the separatrix and target temperatures are almost equal. At low upstream density ($n_u = 3\mathrm{e}19\,\mathrm{m}^{-3}$) the target temperature is much too high for considerations of plate sputtering and at higher upstream density ($n_u = 6\mathrm{e}19\,\mathrm{m}^{-3}$) the separatrix temperature is too low for good core confinement.

Long connection length, $L_c \sim 100$ m, allows a substantial temperature drop in the SOL flux tube as shown in figures 10 and 11. At the high input power of 10 MW, deuterium solutions with $T_{et} \sim 20$ eV and $T_{sep} \sim 120$ eV are possible at a separatrix density of 6e19 m^{-3} (figure 10). Even at a lower density, 3e19 m^{-3}, solutions with $T_{et} \sim 30$ eV and $T_{sep} > 100$ eV are possible with 5 MW of input power (figure 11).

Comparison of the analytical results in figures 10 and 11 with the field-line tracing results in figure 9 give an indication that the NCSX design may produce an attractive SOL regime although detailed three-dimensional modelling is required to draw quantitative conclusions. A majority of the field lines traced satisfy the qualitative criterion of $L_c > \sim 100$ m, assuming that the diffused field-line length will give an indication of the L_c. Future detailed modelling should focus on the subset of the SOL field lines that intersect the proposed target structures in the NCSX design. Once the design is finalized, we can follow these intersecting lines backwards without diffusion to estimate a true L_c.

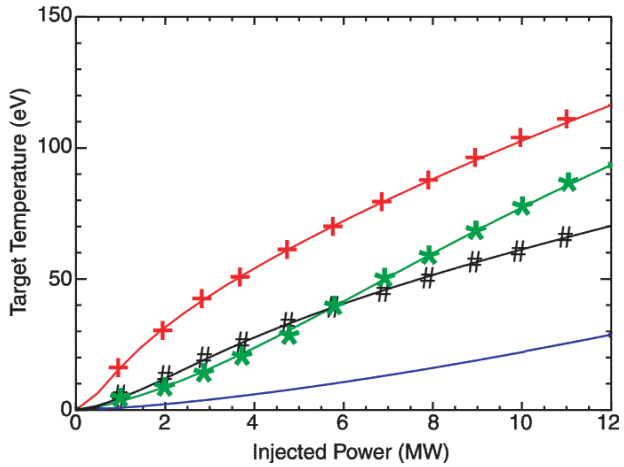

Figure 10. Target temperature vs injected power for four deuterium plasma cases: (a) (red +) symbols use $L_c = 5$ m, $n_u = 3e19$; (b) (black #) symbols use $L_c = 5$ m, $n_u = 6e19$; (c) (green $*$) symbols use $L_c = 100$ m, $n_u = 3e19$ and (d) (blue) plain line uses $L_c = 100$ m, $n_u = 6e19$.

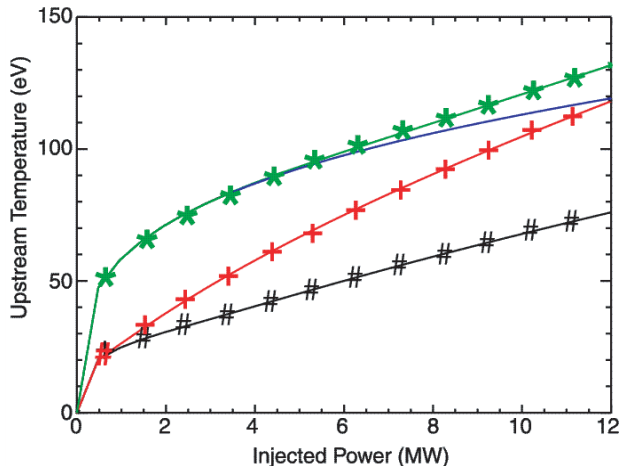

Figure 11. Upstream temperature vs injected power for four deuterium plasma cases: (a) (red +) symbols use $L_c = 5$ m, $n_u = 3e19$; (b) (black #) symbols use $L_c = 5$ m, $n_u = 6e19$; (c) (green $*$) symbols use $L_c = 100$ m, $n_u = 3e19$ and (d) (blue) plain line uses $L_c = 100$ m, $n_u = 6e19$.

5.3. *Implications of short vs long connection length*

Separatrix T_e in the 40 eV range with carbon impurity can lead to thermal instability. As indicated in figure 12, the carbon cooling curve increases sharply with decreasing T_e from 40 eV down to about 7 eV.

If this instability occurs around the LCMS the expected result is a high density, low temperature mantle that is strongly radiating at the edge of the core plasma. If the temperature profile of the core plasma is stiff, as it is in tokamaks, then low separatrix temperature will produce low core confinement.

In diverted tokamaks the effect of this carbon thermal instability is observed in experiments with heavy gas injection to high density [19]. As the density in the SOL increases the temperature drops and the carbon radiation in the SOL increases somewhat with no appreciable decrease in core confinement. However, when the temperature at the separatrix is reduced to about 40 eV, the carbon radiation is observed to move rapidly inside the separatrix and the core confinement is reduced by a factor of two.

A long connection length allows a substantial temperature difference to be established between upstream separatrix temperature and the target temperature. The separatrix temperature can be consistent with good core confinement while at the same time the target temperature can be consistent with low physical sputtering of carbon targets. The physical sputtering curve for deuterium on carbon is given in [17], p 119. For the long L_c solution at $P_{inj} = 6$ MW and $n_u = 5e19$, $T_{et} \sim 10$ eV and the carbon sputtering is a factor of three less than would be the case with short L_c and $T_{et} \sim 40$–60 eV.

Another advantage of long connection length is that most of the temperature drop occurs near the target so the core plasma is screened from incoming neutrals by ionization in the hot plasma not far from the target. This leads to high recycling conditions near the target at moderate core density

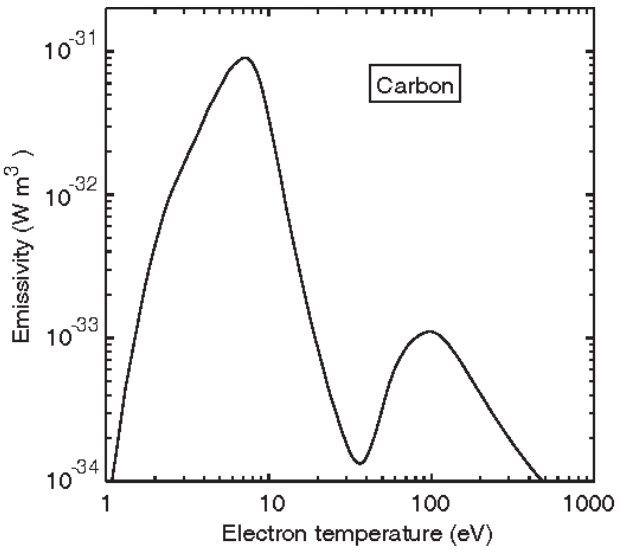

Figure 12. Carbon emissivity (ε) vs electron temperature showing emissivity increase with decreasing temperature in the range 7 eV $< T_e <$ 40 eV. Radiated power is $\varepsilon n_e n_c$.

and can even lead to detachment and substantial reduction of the heat flux on the target at higher core density.

Strong temperature gradients near the target can lead to a transport of impurities away from the targets by the ∇T_i force. However, the high recycling solution typically also generates sufficient flow towards the targets that the drag force on impurities balances the ∇T_i force and impurities are reasonably well entrained near the target surface. Shaping of structures in the vicinity of the targets can help entrain the impurities.

6. Conclusions

We have analysed the suitability of a candidate NCSX boundary configuration for divertor operation. The magnetic fields were calculated with a combination of the MFBE and VMEC codes. Poincaré plots generated with a field-line tracing code demonstrate that the magnetic configuration meets some principal conditions necessary for successful divertor operation. Diffusive effects are studied in addition to field-line tracing with no diffusion. For the case of no diffusion and no limiting surface, field lines launched at the midplane of the bean-shaped cross section ($\phi = 0$) show an accumulation of punctures at the top and bottom of the cross section. The field outside the LCMS seems to be highly stochastic without any discernible island structures. (It is possible that the stochasticity could be reduced by either more resolution in the number of toroidal planes used for the VMEC and MFBE solutions, or the application of various procedures to control the production of magnetic islands [15]. This is left for future studies). Between the midplane and the top and bottom of the $\phi = 0$ cross section there is a flux expansion of a factor larger than 5. The areas near the clusters of punctures in the bean-shaped cross section seem to be suited for placing divertor structures such as divertor plates for intercepting the power and most of the particle flux as well as additional baffles for confining neutrals.

For the purpose of determining the location of protective armour, a proposed limiting surface has been introduced for NCSX. This paper describes a technique for rapidly calculating the three-dimensional plasma footprint on such a limiting surface. Using this technique, the magnetic field topology inside and outside the plasma boundary region for this candidate NCSX configuration of $\beta = 4\%$ is calculated in detail. Diffusion effects are included in these field-line tracing calculations. We provide three-dimensional renditions of the footprints that can be used for design optimization. We also study the correlation of the strike-point locations with diffusion coefficient and angle of incidence upon the surface. Strike points that possess an undesirably large angle of incidence occur in localized groups, indicating that design optimization to reduce the number of such points should be possible. We infer that with an appropriately designed vacuum vessel, connection lengths between the LCMS and plasma-facing components can be made long enough ($\sim$100 m) to ensure sufficient electron temperature gradients between the divertor plates and the separatrix. Finally, we discuss the implications of the field-line connection length on temperature gradients in the SOL and on potential radiation instabilities.

Acknowledgments

We would like to thank Betsy Foote of Livermore Computing for help with the three-dimensional graphics. We also thank members of the NCSX design team who contributed input data especially Long-Poe Ku who provided the VMEC solutions and Art Brooks who provided the first wall data. Finally, we thank John Johnson for his support of this work and of the stellarator effort in general. Work by the Lawrence Livermore National Laboratory was performed under the auspices of the US Department of Energy by the University of California under contract No W-7405-Eng-48.

Appendix

Table 1 contains the Fourier coefficients used to specify the bounding surface (as described in section 2 of the main text).

Table 1.

m	n	$R(m,n)$	$Z(m,n)$	m	n	$R(m,n)$	$Z(m,n)$	m	n	$R(m,n)$	$Z(m,n)$	m	n	$R(m,n)$	$Z(m,n)$
0	0	1.39E+00	0.00E+00	4	5	−7.69E−05	7.78E−05	8	10	−1.31E−05	2.21E−05	12	15	−1.20E−06	−1.66E−06
0	−1	−1.07E−02	1.36E−02	4	4	2.73E−04	−2.01E−04	8	9	−5.80E−06	1.99E−05	12	14	−2.68E−06	−5.57E−06
0	−2	−1.45E−03	1.14E−02	4	3	7.86E−07	−8.62E−06	8	8	1.45E−05	−5.58E−06	12	13	−2.79E−06	−4.74E−06
0	−3	3.16E−03	−3.99E−04	4	2	6.08E−04	−5.13E−04	8	7	2.14E−05	−3.20E−05	12	12	−6.16E−07	−1.67E−07
0	−4	−4.58E−04	2.11E−03	4	1	−3.42E−04	2.29E−04	8	6	3.00E−05	−5.07E−05	12	11	8.46E−07	5.24E−06
0	−5	−3.52E−04	4.37E−04	4	0	3.47E−03	1.54E−03	8	5	−8.21E−07	−3.23E−05	12	10	2.84E−06	6.80E−06
0	−6	−2.43E−04	−6.35E−04	4	−1	−5.77E−03	1.05E−02	8	4	9.43E−06	−7.91E−06	12	9	−4.42E−07	4.60E−06
0	−7	5.89E−06	−1.04E−03	4	−2	5.58E−03	−2.49E−03	8	3	−3.04E−05	4.19E−05	12	8	−7.35E−07	−1.94E−06
0	−8	2.12E−04	−6.73E−04	4	−3	7.73E−05	−8.29E−04	8	2	1.35E−05	5.69E−05	12	7	−8.14E−06	−5.77E−06
0	−9	2.63E−04	2.82E−05	4	−4	−1.76E−04	−1.76E−06	8	1	−1.39E−04	3.12E−05	12	6	−2.03E−06	−7.39E−06
0	−10	1.57E−04	5.85E−04	4	−5	−7.89E−04	7.53E−04	8	0	1.71E−04	−4.41E−04	12	5	−8.76E−06	1.15E−06
0	−11	−1.79E−05	6.89E−04	4	−6	5.55E−07	1.72E−05	8	−1	−6.35E−05	−8.54E−04	12	4	9.06E−06	7.80E−06
0	−12	−1.43E−04	3.33E−04	4	−7	2.69E−04	−2.23E−04	8	−2	3.99E−05	−1.36E−03	12	3	−2.20E−05	1.85E−05
0	−13	−1.45E−04	−1.95E−04	4	−8	2.39E−04	−2.04E−04	8	−3	1.14E−04	−5.53E−04	12	2	8.94E−06	6.10E−06
0	−14	−3.17E−05	−4.89E−04	4	−9	5.99E−05	−6.19E−05	8	−4	−2.24E−04	−1.36E−05	12	1	8.70E−06	1.46E−06
0	−15	9.33E−05	−4.10E−04	4	−10	−1.64E−04	1.32E−04	8	−5	4.82E−05	1.46E−04	12	0	2.12E−04	7.16E−05
1	15	−1.10E−04	−2.06E−04	4	−11	−2.68E−04	2.28E−04	8	−6	−1.45E−04	−7.73E−05	12	−1	1.14E−04	1.38E−04
1	14	2.11E−04	−1.20E−04	4	−12	−2.04E−04	1.81E−04	8	−7	4.74E−05	−3.88E−05	12	−2	−1.33E−04	1.28E−04
1	13	3.63E−04	5.65E−05	4	−13	−3.88E−05	4.31E−05	8	−8	−4.22E−05	6.60E−05	12	−3	−4.75E−06	1.49E−04
1	12	2.14E−04	1.98E−04	4	−14	1.06E−04	−8.37E−05	8	−9	4.47E−07	2.85E−05	12	−4	−1.61E−05	2.05E−04

Table 1. (Continued)

m	n	$R(m,n)$	$Z(m,n)$	m	n	$R(m,n)$	$Z(m,n)$	m	n	$R(m,n)$	$Z(m,n)$	m	n	$R(m,n)$	$Z(m,n)$
1	11	−1.75E−04	1.84E−04	4	−15	1.40E−04	−1.19E−04	8	−10	1.83E−05	−3.21E−06	12	−5	5.20E−06	1.37E−04
1	10	−5.33E−04	−6.74E−06	5	15	2.91E−05	1.31E−05	8	−11	2.53E−05	−3.41E−05	12	−6	3.45E−05	1.05E−05
1	9	−6.10E−04	−2.60E−04	5	14	8.33E−05	−2.63E−05	8	−12	2.08E−05	−4.65E−05	12	−7	−4.82E−06	5.14E−06
1	8	−2.83E−04	−4.14E−04	5	13	7.68E−05	−4.71E−05	8	−13	4.25E−06	−2.91E−05	12	−8	1.71E−05	1.03E−05
1	7	2.66E−04	−3.34E−04	5	12	9.85E−06	−3.16E−05	8	−14	−9.41E−06	−8.29E−07	12	−9	−1.06E−05	1.28E−05
1	6	6.90E−04	−3.64E−05	5	11	−6.63E−05	7.36E−06	8	−15	−1.24E−05	1.96E−05	12	−10	4.18E−06	−1.02E−05
1	5	5.34E−04	3.41E−04	5	10	−9.01E−05	3.93E−05	9	15	2.07E−06	−1.54E−05	12	−11	−8.11E−06	−7.33E−06
1	4	−5.73E−04	4.83E−04	5	9	−3.73E−05	4.15E−05	9	14	−2.51E−06	−1.34E−05	12	−12	−4.79E−06	−6.08E−06
1	3	−7.79E−04	3.31E−05	5	8	7.75E−05	−1.35E−06	9	13	−6.35E−06	−7.96E−07	12	−13	−2.67E−06	1.73E−06
1	2	−5.90E−03	1.36E−03	5	7	1.66E−04	−5.32E−05	9	12	−5.37E−06	1.18E−05	12	−14	3.48E−07	7.81E−06
1	1	1.44E−02	7.24E−03	5	6	1.78E−04	−9.33E−05	9	11	−2.07E−06	1.66E−05	12	−15	1.78E−06	8.57E−06
1	0	3.22E−01	5.13E−01	5	5	6.21E−05	−7.09E−05	9	10	3.69E−06	8.32E−06	13	15	1.42E−06	−1.92E−06
1	−1	−1.37E−01	1.59E−01	5	4	−8.82E−05	−1.49E−05	9	9	2.56E−06	−5.77E−06	13	14	1.85E−06	2.05E−06
1	−2	7.31E−03	−1.18E−02	5	3	−1.64E−04	1.73E−04	9	8	1.77E−06	−1.86E−05	13	13	6.84E−07	4.54E−06
1	−3	4.61E−04	−1.21E−03	5	2	−3.21E−04	1.89E−04	9	7	−1.02E−05	−1.62E−05	13	12	2.10E−08	3.28E−06
1	−4	3.74E−05	−1.27E−04	5	1	4.44E−04	2.18E−04	9	6	−8.55E−06	−4.52E−06	13	11	−1.90E−06	−3.60E−07
1	−5	8.24E−04	5.11E−05	5	0	3.36E−04	−2.93E−03	9	5	−2.28E−05	2.12E−05	13	10	−3.28E−08	−4.61E−06
1	−6	3.55E−04	2.98E−04	5	−1	1.84E−03	−1.45E−03	9	4	−1.75E−07	2.37E−05	13	9	−4.10E−07	−4.73E−06
1	−7	−3.32E−04	2.63E−04	5	−2	4.62E−04	−3.31E−03	9	3	−2.59E−05	2.37E−05	13	8	4.69E−06	−2.47E−06
1	−8	−6.95E−04	−1.44E−06	5	−3	−9.65E−06	−7.77E−04	9	2	2.79E−05	−1.97E−05	13	7	2.17E−06	4.00E−06
1	−9	−6.12E−04	−2.58E−04	5	−4	3.24E−04	5.24E−04	9	1	5.31E−05	−2.15E−07	13	6	7.56E−06	6.39E−06
1	−10	−2.03E−04	−3.37E−04	5	−5	9.79E−04	−8.94E−04	9	0	4.41E−05	2.11E−04	13	5	−4.42E−06	7.66E−06
1	−11	2.27E−04	−2.19E−04	5	−6	9.87E−05	−1.44E−04	9	−1	−1.57E−04	5.83E−04	13	4	8.04E−06	−2.15E−06
1	−12	4.15E−04	−3.83E−06	5	−7	−1.08E−04	1.34E−05	9	−2	−5.59E−04	6.32E−04	13	3	−7.61E−06	−2.14E−06
1	−13	2.64E−04	1.56E−04	5	−8	−1.55E−04	8.34E−05	9	−3	−1.00E−04	7.07E−04	13	2	1.13E−05	−7.95E−06
1	−14	−6.61E−05	1.57E−04	5	−9	−6.26E−05	6.94E−05	9	−4	−2.98E−04	4.72E−04	13	1	−2.56E−05	−7.52E−06
1	−15	−3.41E−04	2.46E−05	5	−10	6.55E−05	1.07E−05	9	−5	2.32E−05	4.23E−05	13	0	9.43E−05	−1.37E−04
2	15	2.13E−04	5.22E−04	5	−11	1.51E−04	−5.81E−05	9	−6	−5.41E−05	−3.99E−05	13	−1	8.75E−05	−1.03E−04
2	14	8.88E−06	4.25E−04	5	−12	1.38E−04	−8.46E−05	9	−7	3.32E−05	6.34E−05	13	−2	7.72E−05	2.96E−05
2	13	−1.96E−04	2.25E−05	5	−13	5.28E−05	−6.00E−05	9	−8	−1.27E−05	1.96E−05	13	−3	1.19E−04	2.55E−05
2	12	−2.72E−04	−4.39E−04	5	−14	−3.97E−05	−8.19E−06	9	−9	7.67E−06	−1.73E−05	13	−4	8.12E−05	−4.27E−05
2	11	−1.26E−04	−5.85E−04	5	−15	−7.97E−05	3.51E−05	9	−10	3.48E−06	−2.85E−05	13	−5	2.33E−05	−6.17E−05
2	10	1.62E−04	−2.55E−04	6	15	2.35E−06	−3.10E−05	9	−11	−7.76E−06	−1.89E−05	13	−6	1.45E−05	−5.76E−05
2	9	3.89E−04	3.83E−04	6	14	−3.16E−05	−2.52E−05	9	−12	−1.33E−05	2.11E−06	13	−7	−2.08E−05	−4.07E−06
2	8	4.11E−04	9.31E−04	6	13	−4.27E−05	−8.08E−07	9	−13	−1.29E−05	2.02E−05	13	−8	8.93E−06	−3.51E−06
2	7	1.33E−04	9.82E−04	6	12	−1.99E−05	2.43E−05	9	−14	−6.33E−06	2.29E−05	13	−9	−5.16E−06	−1.24E−05
2	6	−2.55E−04	3.66E−04	6	11	1.79E−05	3.22E−05	9	−15	6.75E−07	1.14E−05	13	−10	8.96E−06	−4.09E−06
2	5	−5.82E−04	−5.95E−04	6	10	4.35E−05	1.48E−05	10	15	−1.87E−06	4.07E−06	13	−11	−7.34E−07	6.86E−06
2	4	−2.24E−05	−1.18E−03	6	9	2.94E−05	−1.52E−05	10	14	−1.85E−06	1.53E−05	13	−12	3.43E−06	6.46E−06
2	3	−6.10E−04	−4.85E−04	6	8	−1.45E−05	−4.27E−05	10	13	−3.66E−07	1.52E−05	13	−13	1.97E−06	4.54E−06
2	2	9.64E−05	−1.42E−03	6	7	−7.31E−05	−3.95E−05	10	12	2.23E−06	3.86E−06	13	−14	7.33E−07	−2.52E−07
2	1	1.47E−02	1.65E−02	6	6	−8.28E−05	−1.71E−05	10	11	2.23E−06	−1.04E−05	13	−15	3.60E−07	−4.39E−06
2	0	1.26E−01	4.58E−02	6	5	−6.77E−05	3.71E−05	10	10	2.79E−06	−1.72E−05	14	14	7.81E−07	7.81E−07
2	−1	9.68E−02	2.17E−02	6	4	4.92E−05	4.44E−05	10	9	−9.54E−07	−9.58E−06	14	13	5.24E−07	5.24E−07
2	−2	2.71E−02	−2.23E−02	6	3	1.92E−05	−1.73E−05	10	8	1.34E−06	6.89E−06	14	11	−1.19E−06	−1.19E−06
2	−3	−5.46E−03	6.56E−03	6	2	2.22E−04	−5.76E−07	10	7	−3.47E−06	2.54E−05	14	10	−1.07E−06	−1.07E−06
2	−4	−2.60E−04	2.58E−03	6	1	−2.26E−04	1.13E−04	10	6	6.78E−06	2.63E−05	14	9	−1.36E−06	−1.36E−06
2	−5	−4.83E−04	9.57E−05	6	0	−2.36E−04	6.18E−04	10	5	−1.44E−06	1.43E−05	14	8	3.25E−07	3.25E−07
2	−6	−4.84E−04	−7.68E−04	6	−1	−3.05E−03	−1.53E−04	10	4	2.10E−05	−1.39E−05	14	7	−6.39E−07	−6.39E−07
2	−7	−1.38E−04	−8.64E−04	6	−2	−1.28E−03	2.88E−03	10	3	−1.84E−05	−1.12E−05	14	6	1.45E−06	1.45E−06
2	−8	2.77E−04	−2.73E−04	6	−3	−6.04E−04	7.83E−04	10	2	6.71E−06	−2.45E−05	14	5	−2.68E−06	−2.68E−06
2	−9	4.26E−04	4.59E−04	6	−4	−3.93E−04	3.59E−04	10	1	−2.42E−05	−4.53E−05	14	4	3.41E−07	3.41E−07
2	−10	3.16E−04	8.32E−04	6	−5	1.54E−04	−4.59E−04	10	0	4.19E−04	−1.68E−04	14	3	−1.09E−05	−1.09E−05
2	−11	4.03E−05	6.80E−04	6	−6	−3.53E−04	3.49E−04	10	−1	4.23E−04	−9.86E−05	14	2	7.66E−07	7.66E−07
2	−12	−2.04E−04	1.64E−04	6	−7	6.22E−05	3.50E−05	10	−2	2.81E−04	2.91E−04	14	1	1.95E−06	1.95E−06
2	−13	−2.66E−04	−3.35E−04	6	−8	8.13E−05	6.18E−06	10	−3	2.87E−04	−1.32E−05	14	0	3.78E−05	3.78E−05
2	−14	−1.19E−04	−4.79E−04	6	−9	5.78E−05	−3.37E−05	10	−4	1.52E−04	−2.39E−04	14	−1	−6.49E−06	−6.49E−06
2	−15	1.04E−04	−2.29E−04	6	−10	−5.44E−06	−5.30E−05	10	−5	1.28E−04	−1.67E−04	14	−2	−7.03E−05	−7.03E−05
3	15	1.64E−04	−1.62E−04	6	−11	−6.28E−05	−3.52E−05	10	−6	3.28E−05	−6.04E−05	14	−3	−4.16E−05	−4.16E−05
3	14	2.22E−04	−2.18E−04	6	−12	−7.86E−05	2.54E−06	10	−7	1.80E−05	1.73E−05	14	−4	−5.96E−05	−5.96E−05
3	13	1.16E−04	−1.13E−04	6	−13	−4.73E−05	3.11E−05	10	−8	6.26E−06	−5.06E−05	14	−5	−3.56E−05	−3.56E−05
3	12	−8.36E−05	8.38E−05	6	−14	2.57E−06	3.49E−05	10	−9	−3.52E−06	−7.97E−06	14	−6	6.48E−06	6.48E−06
3	11	−2.30E−04	2.25E−04	6	−15	3.70E−05	1.43E−05	10	−10	−1.88E−06	1.07E−05	14	−7	−2.69E−06	−2.69E−06
3	10	−1.99E−04	1.93E−04	7	15	−1.61E−05	2.03E−05	10	−11	−3.83E−06	2.82E−05	14	−8	1.81E−06	1.81E−06
3	9	1.41E−05	−1.84E−05	7	14	−7.52E−06	3.61E−05	10	−12	2.50E−06	2.50E−05	14	−9	−6.33E−06	−6.33E−06
3	8	2.94E−04	−2.93E−04	7	13	6.35E−06	2.59E−05	10	−13	5.85E−06	7.79E−06	14	−10	3.89E−06	3.89E−06
3	7	4.39E−04	−4.32E−04	7	12	1.42E−05	−3.42E−06	10	−14	6.70E−06	−1.02E−05	14	−12	3.46E−07	3.46E−07
3	6	3.32E−04	−3.23E−04	7	11	1.03E−05	−2.95E−05	10	−15	4.18E−06	−1.73E−05	14	−13	−1.19E−06	−1.19E−06
3	5	−3.29E−05	3.53E−05	7	10	−4.21E−07	−3.33E−05	11	15	3.43E−06	4.40E−06	14	−14	−2.01E−06	−2.01E−06
3	4	−4.04E−04	3.91E−04	7	9	−1.46E−05	−5.86E−06	11	14	6.24E−06	−1.35E−06	14	−15	−1.83E−06	−1.83E−06
3	3	3.05E−05	−4.05E−05	7	8	−1.27E−05	3.32E−05	11	13	3.85E−06	−6.34E−06	15	15	9.43E−07	9.43E−07
3	2	−5.52E−04	4.62E−04	7	7	−7.51E−06	6.46E−05	11	12	−6.27E−07	−7.07E−06	15	13	−1.09E−06	−1.09E−06
3	1	2.60E−03	−2.51E−03	7	6	1.75E−05	5.32E−05	11	11	−6.39E−06	−1.98E−06	15	12	−9.20E−07	−9.20E−07
3	0	−1.12E−02	8.83E−03	7	5	1.52E−05	1.94E−05	11	10	−5.57E−06	3.50E−06	15	11	−4.34E−07	−4.34E−07
3	−1	−3.22E−04	−3.33E−03	7	4	2.26E−05	−4.17E−05	11	9	−3.15E−06	6.88E−06	15	10	1.29E−06	1.29E−06

Table 1. (Continued)

m	n	$R(m,n)$	$Z(m,n)$	m	n	$R(m,n)$	$Z(m,n)$	m	n	$R(m,n)$	$Z(m,n)$	m	n	$R(m,n)$	$Z(m,n)$
3	−2	−1.09E−02	1.11E−02	7	3	−4.69E−05	−4.08E−05	11	8	6.72E−06	2.40E−06	15	9	1.22E−06	1.22E−06
3	−3	−3.02E−03	3.05E−03	7	2	−5.52E−05	−7.75E−05	11	7	7.37E−06	−4.67E−06	15	8	2.02E−06	2.02E−06
3	−4	3.27E−03	−3.27E−03	7	1	1.02E−04	−4.28E−05	11	6	1.27E−05	−1.45E−05	15	7	−5.19E−07	−5.19E−07
3	−5	3.33E−04	−3.24E−04	7	0	7.74E−04	7.61E−05	11	5	−6.70E−06	−1.30E−05	15	6	3.29E−07	3.29E−07
3	−6	−1.73E−04	1.74E−04	7	−1	1.01E−03	−1.53E−04	11	4	4.01E−07	−1.11E−05	15	5	−3.41E−06	−3.41E−06
3	−7	−3.70E−04	3.62E−04	7	−2	5.91E−04	3.92E−04	11	3	−2.06E−05	−1.59E−06	15	4	2.87E−06	2.87E−06
3	−8	−2.80E−04	2.71E−04	7	−3	9.29E−04	−7.29E−04	11	2	1.39E−05	7.40E−06	15	3	−1.54E−06	−1.54E−06
3	−9	2.43E−05	−2.87E−05	7	−4	2.11E−04	−2.63E−04	11	1	−2.04E−05	4.43E−05	15	2	5.43E−06	5.43E−06
3	−10	2.95E−04	−2.93E−04	7	−5	3.33E−04	1.54E−04	11	0	−7.91E−05	4.22E−06	15	1	−5.11E−06	−5.11E−06
3	−11	3.59E−04	−3.54E−04	7	−6	−9.69E−05	1.60E−04	11	−1	−1.81E−04	−1.51E−04	15	0	6.52E−05	6.52E−05
3	−12	2.10E−04	−2.05E−04	7	−7	1.16E−04	−1.48E−04	11	−2	−1.63E−04	−3.71E−04	15	−1	5.37E−05	5.37E−05
3	−13	−2.74E−05	2.87E−05	7	−8	−2.15E−05	−4.05E−05	11	−3	−3.98E−05	−3.22E−04	15	−2	1.34E−05	1.34E−05
3	−14	−1.86E−04	1.83E−04	7	−9	−3.04E−05	−3.96E−06	11	−4	−1.35E−04	−2.10E−04	15	−3	2.64E−05	2.64E−05
3	−15	−1.74E−04	1.70E−04	7	−10	−2.70E−05	4.13E−05	11	−5	−4.17E−05	3.32E−05	15	−4	3.49E−05	3.49E−05
4	15	−8.23E−05	6.30E−05	7	−11	−9.28E−06	6.36E−05	11	−6	−4.52E−05	3.88E−05	15	−5	2.40E−05	2.40E−05
4	14	−1.57E−04	1.31E−04	7	−12	1.37E−05	4.43E−05	11	−7	−3.10E−05	1.75E−05	15	−6	2.03E−05	2.03E−05
4	13	−1.17E−04	1.03E−04	7	−13	2.46E−05	4.75E−06	11	−8	−1.95E−06	−1.25E−05	15	−7	−4.71E−06	−4.71E−06
4	12	1.64E−05	−5.97E−06	7	−14	1.86E−05	−2.68E−05	11	−9	−1.15E−05	2.27E−05	15	−8	3.51E−06	3.51E−06
4	11	1.41E−04	−1.13E−04	7	−15	1.55E−06	−3.14E−05	11	−10	1.19E−05	2.41E−06	15	−9	2.03E−06	2.03E−06
4	10	1.61E−04	−1.35E−04	8	15	7.97E−06	2.60E−06	11	−11	8.48E−06	−3.48E−06	15	−10	3.68E−06	3.68E−06
4	9	3.61E−05	−3.57E−05	8	14	1.54E−05	−1.74E−05	11	−12	6.19E−06	−1.31E−05	15	−11	−2.14E−06	−2.14E−06
4	8	−1.61E−04	1.29E−04	8	13	1.15E−05	−2.48E−05	11	−13	−1.05E−06	−1.38E−05	15	−12	−8.56E−07	−8.56E−07
4	7	−3.12E−04	2.59E−04	8	12	4.44E−07	−1.44E−05	11	−14	−6.09E−06	−7.03E−06	15	−13	−7.25E−07	−7.25E−07
4	6	−2.72E−04	2.34E−04	8	11	−1.22E−05	7.69E−06	11	−15	−6.33E−06	1.53E−06	15	−15	1.34E−06	1.34E−06

References

[1] Strumberger E. 1992 *Nucl. Fusion* **32** 737
[2] Strumberger E. 1996 *Nucl. Fusion* **36** 891
[3] Strumberger E. 1996 *Contrib. Plasma Phys.* **36** 171
[4] Kisslinger J. *et al* 1994 *21st EPS (Montpellier, 1994)* vol 18B, I, p 368
[5] Kisslinger J. *et al* 1995 *22nd EPS (Bournemouth, 1995)* vol 19C, III, p 149
[6] Strumberger E. 1997 *Nucl. Fusion* **37** 19
[7] Hirshman S.P. *et al* 1986 *Comput. Phys. Commun.* **43** 143
[8] Nührenberg J. *et al* 1993 *Proc. 14th Int. Conf. on Plasma Physics and Controlled Nuclear fusion Research (Würzburg, 1992)* vol 2 (Vienna: IAEA) p 449
[9] Grossman A. *et al* 2000 *Bull. Am. Phys. Soc.* **45** 172
[10] Zarnstorff M. *et al* 2000 *Bull. Am. Phys Soc.* **45** 170
[11] Hudson S.R., Monticello D.A. and Reiman A.H. 2001 *Phys. Plasmas* **8** 3377
[12] Shafranov V.D. and Zakharov L.E. 1972 *Nucl. Fusion* **12** 599
[13] Strumberger E. *et al* 2002 *Nucl. Fusion* **42** 827
[14] Keilhacker M. *et al* 1982 *Phys. Scr.* T2/2 443
[15] Fujiwara M. *et al* 2001 *Nucl. Fusion* **41** 1355
[16] Grigull P. *et al* 2001 *Plasma Phys. Control. Fusion* **43** 175
[17] Stangeby P.C. 2000 *The Plasma Boundary of Magnetic Fusion Devices* (Bristol: IoP Publishing)
[18] McCormick K 1999 *Proc. 12th Int. Stellarator Conf. on Edge Diagnostic Overview for the W7-AS Divertor Phase (Madison)* Private communication
[19] Petrie T.W. *et al* 1997 *J. Nucl. Mater.* **241–243** 639–44